Digital Image Correlation Development for the Study of Materials Including Multiple Crossing Cracks

Valery Valle, S. Hedan, P. Cosenza, A.L. Fauchille, M. Berdjane

To cite this version:

Valery Valle, S. Hedan, P. Cosenza, A.L. Fauchille, M. Berdjane. Digital Image Correlation Development for the Study of Materials Including Multiple Crossing Cracks. Experimental Mechanics, 2015, 55 (2), pp.379-391. ⟨10.1007/s11340-014-9948-1⟩. ⟨hal-01269981⟩

HAL Id: hal-01269981

https://hal.science/hal-01269981v1

Submitted on 3 Oct 2023

DIGITAL IMAGE CORRELATION DEVELOPMENT FOR THE STUDY OF MATERIALS INCLUDING MULTIPLE CROSSING CRACKS

Valéry VALLE[a]

Stephen HEDAN[b]

Philippe COSENZA[b]

Anne-Laure FAUCHILLE[b]

Mohand BERDJANE[a]

[a] - Université de Poitiers, CNRS UPR 3346 Institut PPRIME

S.P. 2 M.I., Bd. M. et P. Curie, Téléport 2, B.P. 30179

86962 Futuroscope Chasseneuil Cedex

[b] - Université de Poitiers, CNRS UMR 7285 IC2MP, HydrASA

Ecole Nationale Supérieure d'Ingénieurs de POITIERS

1 rue Marcel Doré, 86022 Poitiers Cedex

Corresponding author:

Valery VALLE

Tel. +33 5 49 49 65 45

Fax. +33 5 49 49 65 04

E-mail: valery.valle@univ-poitiers.fr

Intended for publication in *Experimental Mechanics.*

Abstract: This study reports on the digital image correlation (DIC) procedure and its limitation in the case of fracture analysis. A comparison of three different algorithms was carried out for the case of crossing cracks. An improvement of the DIC procedure was proposed to solve the uncertainty problems at the vicinity of the junction of two cracks. This procedure was proposed to perform an evaluation of the displacement when multiple cracks are present in the subset. It was developed using classical minimization process, including Heaviside functions in the kinematical field representation. Some tests were performed to demonstrate the performances of this new algorithm. An application of the multiple fractures on Argillite rock is shown to validate the efficiency and the robustness of the proposed method.

Keywords :

digital image correlation, fracture, multiple cracks, crack crossing, full field measurement, rock.

Introduction:

Optical measurement methods are widely employed in experimental mechanics to characterize the behavior of materials. Some of these methods provide direct access to the experimental kinematical field without contact [1-5]. Moreover, for some of these methods, it is not even necessary to prepare the specimen surface [6]. Among such optical methods, the digital image correlation (DIC) procedure was developed to provide more accurate measurements [7-10], and studies have been conducted to offer an assessment of this method [11]. Many studies have employed this method in the field of fracture mechanics [12-20]. To determine precisely kinematical fields in the neighborhood of the crack and to evaluate its position, some methods have been specially developed. Some of them use a local approach like the point-wise method [21] which uses a genetic algorithm to treat each pixel separately, and the subset splitting method [22] which cuts the subset in two parts. Another method, the eXtended DIC method [23] is based on

X-FEM developments using a global approach. In this last development, the properties of Heaviside functions are employed to solve the problem of kinematical discontinuities. Other developments have been fulfilled in the aim to perform an accurate determination of the crack position [18-20]. However the experimental study of multiple growing and crossing cracks localization is generally treated using a classical DIC algorithm and discarding data near discontinuities [14].

In this paper, it is proposed to use Heaviside function properties in the case of a local approach (subset based), and in the aim to determine both kinematical field and crack position when multiple discontinuities are in one subset and to bring an answer for the multiple crossing cracks localization issue.

The aims of this paper can be developed as:

- A novel approach is proposed, the Heaviside-based DIC method (H^k-DIC where k is the number of cracks in one subset), to address the cases of multiple cracks and crack crossing in a subset.
- A comparison between a classical DIC method, and the new algorithm (H^1-DIC) is proposed on synthetic images representing a single crack (opening Mode I and sliding Mode II).
- A validation of the crack localization with H^1-DIC is presented on synthetic images representing a circular single crack.
- A comparison between the new proposed algorithms (H^1-DIC and H^2-DIC) is shown on synthetic images representing a crack crossing.
- An application on the study of fractured clay rock in underground gallery is presented using a natural speckle. The crack network is connected and composed of two types of fractures: (a) sub-horizontal cracks and (b) sub-vertical cracks.

1 Heaviside-based DIC (H^k-DIC).

The proposed method is an extension of the classical DIC method. It has been chosen to develop this process using a local approach to clearly separate metrological problems from finite element ones. Actually, two methods based on local approach have been described in literature. The point-wise method [21] which can capture cracks but is computationally expensive due to a large number of unknowns. The subset-splitting technique [22] which is simpler, cannot handle more than one crack. The proposed method has been established using classical developments [7-9] (i.e. a minimization process on a subset). For sub-pixel evaluation, the bi-cubic image interpolation algorithm was selected. The correlation function *S* is described using a classical representation where *F* and *G* are the initial and the final images respectively.

$$S\left(u, v, \frac{du}{dx}, \frac{du}{dy}, \frac{dv}{dx}, \frac{dv}{dy}\right) = 1 - \frac{\int_S F(x,y)G(x^*,y^*)dxdy}{\sqrt{\int_S (F(x,y)-\overline{F_S})^2 dxdy \int_S (G(x^*,y^*)-\overline{G_S})^2 dxdy}} \tag{1}$$

$$\text{With } x^* = x - u - \frac{du}{dx}x - \frac{du}{dy}y \quad \text{and} \quad y^* = y - v - \frac{dv}{dx}x - \frac{dv}{dy}y \tag{2}$$

The kinematical transformation is defined by simple in-plane translations (u, v) and the first gradients ($\frac{du}{dx}, \frac{du}{dy}, \frac{dv}{dx}, \frac{dv}{dy}$).

To be able to accurately determine displacements in presence of a crack in the subset, the kinematical field was enriched by adding Heaviside functions as in the spirit of the extended digital image correlation method [23]. However the algorithm was developed as a local approach and offers a treatment on a subset. The kinematical field was defined to represent kinematical jumps along a straight line following the development of the subset splitting method [22]. However, the proposed technique differs from the previously cited by many points.

- The kinematical field can be described by:

$$x^* = x - u - \frac{du}{dx}x - \frac{du}{dy}y - \sum_k u_k H_k(x,y)$$

$$y^* = y - v - \frac{dv}{dx}x - \frac{dv}{dy}y - \sum_k v_k H_k(x,y) \qquad (3)$$

Figure 1, equations 4 and 5 show the description of the two-dimensional Heaviside function. When k is equal to 1, the proposed field is adapted to analyze subsets with one crack. For k=2, the field is well adapted to represent two cracks, with or without crossing or branch. k>2 can be used to retrieved kinematical field in particular cases like multiple branch crack studies.

- To ensure a correct measurement in any crack orientations, the straight line representing the crack was defined by its polar coordinates and can be described in Figure 1 and by:

$$H_k(x,y) = H_k(r_k, \theta_k, r) \qquad (4)$$

$$H_k(x,y) = H_k(x\,cos(\theta_k) + y\,sin(\theta_k) - r_k) = H_k(r - r_k)$$

$$\text{and} \quad H_k(x,y) = 0 \text{ if } r \le r_k$$

$$H_k(x,y) = 1 \text{ if } r > r_k \qquad (5)$$

where r_k and θ_k define the position and the orientation of the two-dimensional Heaviside function H_k.

- The subset was treated as a unique field using a set of k two-dimensional Heaviside functions $H_k(x, y)$ associated with k jump vectors (u_k, v_k). All subsets were enriched. u_k *and* v_k approach zero when there is no discontinuity in the subset. Contrarily to standard DIC algorithm which cannot ensure solution unicity when a discontinuity is present in the subset, this approach gives a unique global solution by subset. This property allows conserving equivalent metrological performances with or without discontinuity in the subset.

- Parameters $(u, v, \frac{du}{dx}, \frac{du}{dy}, \frac{dv}{dx}, \frac{dv}{dy}, u_k, v_k, \theta_k, r_k)$ were minimized in a single process. As other DIC algorithms, before optimization, initial values were calculated by a minimization process to ensure an optimization start near the global solution.
- The optimization process, based on a Newton algorithm, was employed to retrieve the displacement at the center of the subset.
- Each subset was treated separately and didn't depend on a "nearest well correlated" subset. Because of displacement discontinuity presence, two spatially nearest data could have displacement values far from each other. The chosen procedure ensures the convergence independency of the algorithm and gives a better robustness (i.e. no a-priori solution). Moreover, the algorithm can be implemented in "Massive Parallel Computation" with a GPU card. In table 1, a comparison of computation rates (Msubset/hour and subset/s) was made using GPU and CPU implementations for a subset dimension of 32x32 pixels^2.

This method was implemented in a software (XCorrel) using a simple graphical interface as in classical DIC software.

A first comparison is proposed using one Heaviside function (k=1). It allows analyzing problems with a single crack in a subset. In a second time, the crack crossing problem is studied using a description with two Heaviside functions (k=2).

2 Testing conditions

As in other works [11], synthetic images were created from different widths of speckle grains, wherein each speckle grain was defined by a half cosine function (Figure 2-a). To accommodate the integration phenomenon of the charge-coupled device (CCD) camera, the initial images were created with a dimension of 3,200×3,200 pixels^2, a displacement was applied to these images, and then, the final images of 320×320 pixels^2 were generated by sub-sampling (Figure 2-b). Each pixel of the final images was calculated by averaging 10×10 pixels^2 of the initial pixels such that a displacement of one pixel is equivalent to 0.1 pixel in the final image. This classical procedure offers a good comparison between algorithms even if it is far from experimental conditions.

To evaluate the quality of the results, the classical local error indicator Φ was employed [24] and described as follow:

$$\Phi^2 = [F(x,y) - G(x^*,y^*)]^2 \tag{6}$$

A pseudo strain indicator $<\varepsilon>$ was calculated for crack detection evaluations and it was defined as a strain in the spirit of Tresca [24]:

$$< \varepsilon >= \frac{|\langle\varepsilon_1\rangle - \langle\varepsilon_2\rangle|}{2} \tag{7}$$

where ε_1 and ε_2 are the principal strains calculated from the displacements field using finite differences between neighborhood subsets.

To show both resolution and spatial resolution at the same time (see Fig 3 and Fig 4), Δu and Δv errors (root mean square: RMS) were calculated by comparing the actual displacement value to the calculated displacement at the center of the subset using:

$$\Delta u = \sqrt{\frac{1}{n}\sum_n \left(u_{r-}u_c\right)^2} \quad \text{and} \quad \Delta v = \sqrt{\frac{1}{n}\sum_n \left(v_{r-}v_c\right)^2} \tag{8}$$

where n is the number of pixels along the y axis of the image, u_r and u_c are respectively real and calculated displacements for opening Mode I, v_r and v_c are respectively real and calculated displacement, for sliding Mode II.

To evaluate the effect of subset sizes, Δu and Δv errors were calculated on two zones using eq 8, where n is the number of pixels on each zone (see Fig 5).

U and V are respectively the perpendicular and parallel displacement jumps at the discontinuity. Last, all results are calculated using a grid step equal to 1 pixel.

3 H^1-DIC evaluations on a single crack

3.1 For different discontinuity jumps.

To quantify the accuracy of each method, the synthetic images corresponding to figure 2 were chosen. It was corresponding to a sliding Mode II (Fig 2-c) and an opening Mode I (Fig 2-d) analyzed with a subset dimension equal to 32×32 pixels^2.

It was proposed to compare the classical DIC algorithm, defined by equations (1) and (2), and the H^1-DIC procedure represented by equations (1) and (3). For this last, k equal to one was chosen.

Figure 3 a) and b) show the evolution of the measurement error for a sliding mode (Mode II) and for parallel displacement jumps V, varying between 0.2 to 2.0 pixels. In these plots, the constant values of errors from each side of the discontinuity (zones 1) can be observed. These different values illustrate the evolution of the well-known systematic errors of the DIC algorithms [11][25]. For Figure 3 a), the central region (zone 2) near the jump has a width equal to the dimension of the subset (32 pixels) and the error depends of the value of the jump V.

Figure 3 b) presents the results obtained using the H^1-DIC algorithm in the same conditions. The spatial resolution is equal to one pixel, and the resolution is equivalent to those obtained with the classical DIC algorithm out of the central region (zone 2).

Figure 3 c) and d) give the contribution of the proposed algorithm for a chosen displacement jump V equal to 1.2 pixels in the case of a sliding Mode II. The local error map Φ shows that the algorithm convergence is better using an appropriate kinematical field. And finally, the pseudo strain map $<\varepsilon>$ demonstrates that using H^1-DIC algorithm, data are valid near the jump. Moreover, the discontinuity is well retrieved.

Figures 4 a) and b) give the evolution of the measurement error for an opening mode (mode I) and for perpendicular displacement jumps U, varying between 0.2 to 2.0 pixels. Errors from each side of the discontinuity (zones 1) have the same values than those obtained for the sliding mode. The central region near the jump (zone 2) has still a width equal to the dimension of the subset (32 pixels) and the error also depends of the value of the jump U. It can be observed that data near the jump (zone 2) are less accurate in this case comparatively to the sliding Mode II (Fig 3-b). This can be connected to the effect of the optical flow violation along the crack. This effect is generated by the appearance of new gray levels constituting the crack.

Figures 4 c) and d) show the contribution of the proposed algorithm for a chosen displacement jump U equal to 1.2 pixels in the case of an opening Mode I. The local error map Φ shows that the algorithm convergence is better using an appropriate kinematical field but less good than for the sliding mode. On Figure 4-d, the effect of the optical flow violation can be better observed. However, the pseudo strain map $<\varepsilon>$ demonstrates that using H^1-DIC algorithm, data are always valid near the jump.

With this first test, it can be concluded that the proposed algorithm gives results with the same quality than others specific developments [21-23].

3.2 For different subset sizes.

In a second test, it was proposed to evaluate the measurement errors for different subset sizes. However, in literature [11-25] it has been confirmed that, in a first order, random errors depend on the subset size and systematic errors depend on the gray level interpolation. To generate random errors, it was so necessary to create noisy images. New sets of synthetic images were generated, including a Gaussian noise of 10% (25 gray levels). The applied noise was chosen different for initial and final images. Displacement jump was chosen equal to 1.2 pixels. Errors Δu and Δv were calculated using equation 8 on zones1 and zones 2.

Figures 5 a) and b) show average errors calculated from different subset size and for a sliding Mode II and an opening Mode I respectively. Zones 1 and zones 2 correspond to those defined in figures 3 and 4.

Globally, the errors are the same in opening Mode I and sliding Mode II. In zones 1, measurement errors show classical evolutions [11]. In presence of noise, H^1-DIC algorithm remains equivalent to DIC algorithm in zone 1, and is more accurate in zones 2 near the displacement discontinuity. Even if the noise is high, the robustness of the proposed algorithm is good.

3.3 For different discontinuity orientations.

A third test corresponding to a crack localization test was presented. In these cases, synthetic images were created generating in a single image, different crack orientations. To mimic a sliding Mode II on the final image, the initial one was rotated in one sense, and a rotation of the central part was applied in the other sense (Figure 6 a). The rotation angle was chosen equal to ±0.23 degree, giving a displacement jump equal to 1.6 pixels along the crack.

Figures 6-b) and c) show the calculated displacement maps and confirm the good performances of the H^1-DIC algorithm comparatively to classical one. The residual error map Φ is plotted and confirms the excellent performances of the algorithm in retrieving the crack position contrarily to classical DIC algorithm. The crack localization can be appreciated on pseudo strain map $<\varepsilon>$ and follows the imposed circular shape.

To mimic an opening Mode I on the final image, a radial strain of 2% was applied on the central part of the initial image (Figure 7-a), giving a maximal displacement jump equal to 1.6 pixels.

On Figures 7-b) and c), the conclusions obtained for the sliding mode can be retrieved: The algorithm convergence is ensured and the position of the crack is well determined contrarily to the classical DIC algorithm.

In these test, the H^1-DIC algorithm appears to be an appropriate procedure to analyze a kinematic field with one crack in the subset. However, in these preliminary tests, the simulated kinematic fields correspond to those included in the formulation of the H^1-DIC algorithm. It would be interesting to examine what occurs when the kinematic field is not simulated with a single straight line crack but when two cracks are present in the observed field. Observations on fractured materials illustrate that the common case found after a single crack, is the intersection of cracks. It was proposed to simulate this case and to investigate how the DIC algorithms can operate in this situation.

4 H^1-DIC and H^2-DIC evaluations on a crossing crack

To mimic the case of multiple cracks in a subset, it was proposed to simulate images with more than one discontinuity. Three zones were created with two of them having an imposed displacement indicated with red arrows in Figure 8 a). One part of this structure can be mechanically considered as a mixed mode of fracture. For these tests, the subset dimension was chosen to be 32×32 pixels² and the imposed displacement was fixed to 0.8 pixel (maximum of each component).

A comparison was proposed between the classical DIC, H^1-DIC and H^2-DIC algorithms. For this last, the kinematical representation of the displacement field is still represented by equation 3, where the problem of crossing cracks can be solved using k=2. Heaviside functions H_1 and H_2 are so defined to represent the kinematical jumps along two straight lines. The combination of two Heaviside functions allows for the representation of up to four kinematical jumps in a subset.

Figure 8 b) illustrates that the classical DIC algorithm is unsuitable for observing multiple cracks and measuring the displacements around the cracks. It can be retrieved that the local error indicator (Φ) is less efficient when the displacement jump is subpixel [24].The pseudo strain map $<\varepsilon>$ gives undetectable displacement jumps.

Figure 8 c) shows the performances of the H^1-DIC method. It can be observed that a very good calculation is obtained for the vertical and horizontal displacement discontinuity edges. However, the H^1-DIC kinematical model cannot retrieve the actual displacement field when the discontinuity crossing is in the subset. The local error map Φ shows some errors along the discontinuity corresponding to the mixed mode (opening and sliding). It can be explained by the opening of the crack lips, generating black pixels in the final image. However, the vertical displacement map v and the pseudo strain map $<\varepsilon>$ illustrate that H^1-DIC method is unable to retrieve displacement at the crack crossing.

The performances of the H^2-DIC algorithm are presented in Figure 8 d). Local error map Φ don't show differences in comparison to the H^1-DIC, confirming that in these two cases, minimization is ensured. The vertical displacement map v and the pseudo strain map $<\varepsilon>$ illustrate the improvement of the discontinuity localization. Displacements are better calculated on the crack intersections using H^2-DIC procedure. This test exhibits that H^2-DIC algorithm is necessary to treat data issued from the crossing of two cracks.

5 Application to argillite rock fracture

As the DIC method is a powerful tool that allows for the measurement of displacement fields without contact, many applications of this method have been published along with an increasing number of reports on the analyses of rock materials [26-30]. In this study, each DIC algorithm presented is compared in the context of fractured clay rocks. DIC was used for the first time in an underground gallery to monitor the desiccation cracks during annual climatic cycles (from March 2011 to present). This experimental in situ investigation was carried out on a study area of 344×275 mm^2, located on the East96 gallery front at the Tournemire experimental station [31], during which the relative humidity (RH) and temperature (T) were measured continuously. Clay rocks are considered in several industrial countries as potential repositories for high-level radioactive wastes. Among the critical issues related to the long-term safety assessment of such geological repositories, the study of the so-called excavation damaged zone (EDZ) is of particular importance. The initiation and extension of the EDZ are governed by many parameters [32-34], such as the material properties of the rock (e.g., material anisotropy), the initial stress field, the existence of natural fracture zones in the rock mass, the geometry of the gallery, and the hydric state existing in the gallery. With regard to the hydric state in the gallery, fractures associated with the desaturation of argillaceous medium have been observed on gallery fronts in several underground research laboratories, e.g., in the experimental platform at Tournemire [35,36] and in the Mont Terri laboratory [37]. This hydric fracturing process is evidenced in situ by sub-horizontal cracks spaced at several decimeters on all vertical walls in contact with the ambient air. The corresponding crack openings can reach a few millimeters in winter (dry state), whereas these cracks are closed in summer (wet state). These cracks are induced by drying and are parallel to the bedding planes, suggesting that they are partially controlled by sedimentological patterns (e.g., vertical differences in sediment granulometry and/or mineral composition). The changes in the crack openings calculated from the displacement fields and the strain fields were clearly correlated and concomitant with changes in RH and T (with 25%<RH<99% and 6°C<T<14°C) in the gallery [29]. Moreover, although the main desiccation cracks were sub-horizontal and associated with the direction of bedding planes, the displacement fields demonstrated the existence of sub-vertical cracks [29]. These two types of desiccation cracks are connected (i.e presence of crack crossings). Globally, the understanding of the 3D hydric exchange requires the measurement of large volume, but also an accurate determination of crack lengths and crack openings. It can be noticed that only full field displacement measurements can give sufficient data to tackle this problem. In-plane experimental displacements (u, v) at a gallery front in the experimental platform of Tournemire can be obtained and the study surface corresponds to the surface orthogonal to the crack propagation (i.e. gallery front in contact with the ambient air) (Figure 9).

Experimentally, it was impossible to mark the surface of the material because it contributes to the exchange of water. The natural roughness of material has been used as natural speckle and allows the DIC method to be employed. The three algorithms presented in this paper (classical DIC, H^1-DIC, and H^2-DIC) were used to compare their performances on this real case. For these comparisons, two images were selected at $t_0=0$ and $t=t_0+1$ month. All these conditions validate the requirement of using new DIC algorithms (H^1-DIC and H^2-DIC). The initial image size is 1,280×1,024 pixels^2 (Figure 9), and calculations are made every pixels, thus yielding a resulting image of 1,240×984 data. The magnitude of the image is equal to 0.269 mm/pixel, and the subset size is 40×40 pixels^2.

Figure 10 presents the displacement maps (u, v) calculated using the classical DIC algorithm. The accuracy of the calculations is high (in regions outside of the cracks). However, the local error map (Φ) and the pseudo strain map ($<\varepsilon>$) show that the discontinuities are not retrieved. The red arrows indicate some crossing crack localizations which are undetectable with this algorithm. The classical DIC method is not appropriate for performing measurements in the presence of single and multiple cracks.

Figure 11 presents the same results obtained using H^1-DIC algorithm. It can be observed on all maps that the noise is still low (u, v), the convergence is ensured (Φ), and globally the cracks are retrieved ($<\varepsilon>$). However, all the details (red arrows) illustrate the crack localization problems encountered when H^1-DIC algorithm has to analyze crossing cracks. These results demonstrate that this method is not well adapted to treat the problem of multiple cracks in the subset, even for a real case.

Figure 12 shows the results obtained from the displacement calculation using the proposed H^2-DIC algorithm. These results show excellent localization of the cracks with high global accuracy. Moreover, it can be seen that the displacement jumps have been retrieved at the crack crossings.

Figure 13 presents displacement profiles, orthogonal to the cracks when a crack crossing is in the subset. The previous conclusions can be retrieved; H^1-DIC algorithm can capture only one discontinuity and H^2-DIC algorithm can measure the displacements at the neighborhoods to the cracks and in presence of a crack crossing in the subsets. Classical DIC algorithm gives a crack opening underestimation higher than 30% because maximum displacements along the crack cannot be reached (Figure 13b) Moreover, it does not allow estimating the location of the sub-vertical crack (Figure 13a). The crack length measurement with H^1-DIC is also underestimated (5% on observed field) and cannot be evaluated using a classical DIC algorithm.

On these plots, two displacement gradients can be observed perpendicularly to sub-horizontal cracks (figure 13-b); the first, placed beyond 25 pixels from cracks, corresponds to data observed in the previous study [29]. The second, near the crack (within 25 pixels from cracks) gives higher values. The hydric exchange of the crack lips can explain the increasing of the strain near the crack.

For the proposed example with a natural speckle, the resolution can be estimated equal to 0.05 pixel, given a resolution near 1/100 mm.

Figure 14 shows the evolution of temperature (T), relative humidity (RH) and the crack aperture of three cracks (two sub-horizontal cracks indexed 1 and 2 (black and red plots, respectively) and one sub-vertical crack (green plot) during seven months (middle of summer to middle of winter). Sub-horizontal crack openings are calculated by subtracting the *v* displacements on both sides of each crack, and by averaging these openings along the crack. Sub-vertical crack openings are obtained by the same way, using *u* displacements. It can be retrieved results of the previous works on clay material in gallery [29]. Sub-horizontal and sub-vertical cracks globally follow the variations of RH and T. Moreover, the evolution of the major sub-horizontal crack (called sub-horizontal 1) and sub-vertical crack is more pronounced: these cracks are closed in summer and their openings are continuous during winter. However, some smaller sub-horizontal cracks (called sub-horizontal 2), not observable in the previous works using a multi-scale DIC algorithm [29], show a different behavior than the major ones: contrary to the major sub-horizontal cracks, these minor sub-horizontal cracks could be closed in winter (compare the evolution of major sub-horizontal crack 1 to that of minor sub-horizontal crack 2 in Figure 14). These differences put in evidence the complexity of behavior and the structure of the argillite and the interpretation of these experimental dataset has emphasized the need for a mechanical multi-scale approach to understand the desiccation cracking mechanisms. These results show the advantages using this new algorithm (H^k-DIC), allowing the measurement of large fields, and giving more accurate data.

These tests have demonstrated that the Heaviside-based DIC methods are very well adapted to the case of fracture analysis. And in the case of field measurements in presence of multiple cracks, the proposed H^2-DIC algorithm is necessary to retrieve displacements near the crack crossings.

Conclusion

After having recalled the principles of the DIC measurement method, it was applied to analyze displacement in the presence of cracks. The authors proposed to develop a novel algorithm (Heaviside-based DIC) based on a local approach (subset base), and to analyze their performances comparing to a classical DIC algorithm. For that, an evaluation process based on synthetic images and on classical indicators was proposed. The first tests related to single crack detection, for different discontinuity jumps values, different crack orientations and different subset sizes. A second test was proposed and concerned the case of crossing cracks. The H^1-DIC method has shown its accuracy for single crack localization but it was insufficient to retrieve the crossing of cracks. Therefore, it was proposed to use a more adapted version of the H^1-DIC method, the H^2-DIC, to address crossing cracks. The H^2-DIC algorithm was based on a displacement field including two Heaviside functions, modulated by two jump vectors. This kinematical representation authorized the displacement field to represent two cracks in the subsets. A first test on a simulated example was presented and exhibits good efficiency of the H^2-DIC method to extract the displacement fields at the neighborhood of cracks, whereas the results far away from the cracks were not affected. Then, an actual case was presented illustrating the performance of each algorithm. The experimental study considered argillaceous medium because this material presents crossing sub-horizontal and sub-vertical cracks. Classical DIC, H^1-DIC, and H^2-DIC methods were compared. In this experimental case, all previous conclusions have been retrieved for each method. The efficiency of the H^1-DIC and H^2-DIC algorithms has been shown, and the requirement of the particular H^2-DIC algorithm to perform measurements in presence of multiple cracks and crack crossings has been demonstrated. A particular application was treated; the measurement of full field displacement on fractured argillite rock was shown. Last, the evolution of sub-horizontal and sub-vertical cracks can be plotted with the evolution of the temperature and the relative humidity, to exhibit their relations. The proposed development demonstrates its efficiency to localize some sub-pixel cracks and to provide more accurate and more local information.

Acknowledgments

The authors would like to express their gratitude to the national program NEEDS (Nucléaire, Energie, Environnement, Déchets, Société) and the French Institute for Nuclear Safety and Radioprotection (IRSN) for supporting and funding this work.

This work pertains to the French Government program “Investissements d’Avenir” (LABEX INTERACTIFS, reference ANR-11-LABX-0017-01)

References

[1] Pfaff R.D., et al., An interpretation of Twyman-Green interferograms from static and dynamic fracture experiments. Int. J.Solids Structures 1995, 32, p 939-955.

[2] Picart P, Diouf B, Lolive E, Berthelot J-M. Investigation of fracture mechanics in resin concrete using spatially multiplexed digital Fresnel holograms. Opt Engng 2004;43(5), p 1169–1176.

[3] Dubois F., Méité M., Pop O., Absi J., Characterization of timber fracture using the Digital Image Correlation technique and Finite Element Method, Engineering Fracture Mechanics, Volume 96, 2012, p 107-121

[4] Hedan S, Valle V, Cottron M, Calculation of J-integrals using experimental and numerical data: Influences of ratio (a/W) and the 3D structure, Engineering Fracture Mechanics, Volume 78, Issue 9, 2011, p 1976-1985

[5] Yoneyama S, Ogawa T, Kobayashi Y, Evaluating mixed-mode stress intensity factors from full-field displacement obtained by optical methods, Engineering fracture mechanics, 74, 2007, p 1399–1412.

[6] Mauroux T, Benboudjema F, Turcry P, Aït-Mokhtar A, Deves O, Study of cracking due to drying in coating mortars by digital image correlation, Cement and Concrete Research, Volume 42, Issue 7, 2012, p 1014-1023

[7] Sutton MA, Wolters WJ, Peters WH, Ranson WF, McNeill SR, Determination of displacements using an improved digital correlation method, Image Vision Comput, 1 (3) 1983, p 133–139

[8] Cheng P, Sutton MA, Schreier HW, McNeill SR, Full-field speckle pattern image correlation with B-spline deformation function, Exp. Mech., 42 (3), 2002, p 344–352

[9] Bruck HA, McNeill SR, Sutton MA, Peters WH. Digital image correlation using Newton–Raphson Method of partial differential correlations. Exp Mech 1989;29:261–7.

[10] Hild F, Raka B, Baudequin M, Roux S, Cantelaube F, Multi-scale displacement field measurements of compressed mineral wool samples by digital image correlation, Appl. Opt., 41 (32) 2002, p 6815–6828

[11] Bornert M, Brémand F, Doumalin P, Dupré J.-C, Fazzini M, Grédiac M, Hild F, Mistou S, Molimard J, Orteu J.-J, Robert L, Surrel Y, Vacher P, Wattrisse B, Assessment of digital image correlation measurement errors: Methodology and results, Experimental Mechanics, 49 (3), 2009, p 353-370

[12] Gonzalez J, Knauss WG, Strain inhomogeneity and discontinuous crack growth in a particulate composite, J Mech Phys Solids, 4610, 1998, p 1981–1995.

[13] Chao YJ, Luo PF, Kalthoff JF, An experimental study of the deformation fields around a propagating crack tip, Experimental Mechanics ,382, 1998, p 79–85.

[14] Helm J Digital image correlation for specimens with multiple growing cracks, Experimental Mechanics, 48, 2008, p753–762.

[15] McNeill SR, Peters WH, Sutton MA, Estimation of stress intensity factor by digital image correlation, Engineering Fracture Mechanics, Volume 28, Issue 1, 1987, p 101-112

[16] Sutton MA, Helm JD, Boone ML, Experimental study of crack growth in thin sheet 2024-T3 aluminum under tension-torsion loading, International Journal of Fracture, 109, 2001, p 285–301.

[17] Wei Z, Deng X, Sutton MA, Yan J, Cheng CS, Zavattieri P, Modeling of mixed-mode crack growth in ductile thin sheets under combined in-plane and out-of-plane loading, Engineering Fracture Mechanics, Volume 78, Issue 17, 2011, p 3082-3101

[18] Fagerholt E, Børvik T, Hopperstad OS, Measuring discontinuous displacement fields in cracked specimens using digital image correlation with mesh adaptation and crack-path optimization, Optics and Lasers in Engineering, Volume 51, Issue 3, 2013, p 299-310.

[19] Grégoire D., Maigre H., Morestin F., New experimental techniques for dynamic crack localization. European Journal of Computational Mechanics, Revue Européenne de Mécanique Numérique, 18(3-4), 2009, p 255-283.

[20] Réthoré J., Hild F., Roux S. Extended digital image correlation with crack shape optimization, International Journal for Numerical Methods in Engineering, 73(2), 2008, p 248-272.

[21] Jin H, Bruck HA, Pointwise digital image correlation using genetic algorithms, Experimental Technique, 291, 2005, p 36–39

[22] Poissant J, Barthelat F, a novel subset splitting procedure for digital image correlation on discontinuous fields, Experimental mechanics, vol 50, 2010, p 353-364.

[23] Réthoré J, Roux S, Hild F, From pictures to extended finite elements: extended digital image correlation (X-DIC), C R Mec, 335, 2007, p 131–137

[24] Réthoré J, Roux S, Hild F, Shear-band capturing using a multiscale extended digital image correlation technique, Comput. Methods Appl. Mech. Engrg., 196, 2007, p 5016–5030

[25] Sutton MA, McNeill SR, Jang J, Babai M, Effects of subpixel image restoration on digital correlation error estimates, Opt Eng, 27 (10), 1988, p 870–877

[26] Yang D, Bornert M, Chanchole S, Wang L, Valli P, Gatmiri B, Experimental investigation of the delayed behavior of unsaturated argillaceous rocks by means of Digital Image Correlation techniques, Applied Clay Science, Volume 54, Issue 1, 2011, p 53-62

[27] Hédan S, Cosenza P, Valle V, Dudoignon P, Fauchille AL, Cabrera J, Experimental investigation of the damage process induced by desiccation and heating in Tournemire argillite using Digital Image Correlation, International Journal of Rock Mechanics and Mining Sciences, A. 2012, vol. 51, 2012, p 64-75

[28] Zhang H, Huang G, Song H, Kang Y, Experimental investigation of deformation and failure mechanisms in rock under indentation by digital image correlation, Engineering Fracture Mechanics, Volume 96, 2012, p 667-675

[29] Hédan, S, Fauchille AL, Valle V, Cabrera J, Cosenza P, one-year monitoring of desiccation cracks at Tournemire experimental station using Digital Image Correlation, International Journal of Rock Mechanics and Mining Sciences, DOI10.1016/j.ijrmms.2014.02.006.

[30] Bésuelle, P, Desrues, J, Raynaud, S, Experimental characterisation of the localisation phenomenon inside a Vosges sandstone in a triaxial cell ,International Journal of Rock Mechanics and Mining Sciences, Volume 37, Issue 8, 2000, p 1223-1237.

[31] Tournemire experimental station, Institut de Radioprotection et de Sureté Nucléaire (IRSN), http://www.irsn.fr/en/research/scientific-tools/experimental-facilities-means/Tournemire/Pages/TOURNEMIRE-experimental-station.aspx

[32] Blümling P, Bernier F, Lebon P, Martin CD, The Excavation-Damaged Zone in clay formations - Time-dependent behaviour and influence on performance assessment, Physics and Chemistry of the Earth, 32, 2007; p 588-599.

[33] Bossard P, Meier MP, Moeri A, Trick T, Major JC. Geological and hydraulic characterisation of the excavation disturbed zone in the Opalinus Clay of the Mont Terri Rock Laboratory, Eng. Geol,.66(1-2), 2002 p 19-38.

[34] Tsang CF, Bernier F, Davies C, Geohydromechanical processes in the Excavation Damaged Zone in crystalline rock, rock salt, and indurated and plastic clays - In the context of radioactive waste disposal, Int. J. of Rock Mech and Min Sci, 42(1), 2005, p 109-125.

[35] Cabrera J, Beaucaire C, Bruno G, De Windt L, Genty A, Ramambasoa N, Rejeb A, Savoye S, Volant P, Projet Tournemire : Synthèse des Résultats des Programmes de Recherche 1995/1999. IRSN Report;2001.

[36] Matray JM, Savoye S, Cabrera J, Desaturation and structure relationships around drifts excavated in the well-compacted Tournemire’s argillite (Aveyron, France), Eng Geol 90, 2007, p 1-16.

[37] Möri A, Bossart P, Matray JM, Franck E, Fatmi H, Ababou R, Mont Terri Project: cyclic deformations in the Opalinus Clay, In: proceedings of the International Meeting of Clay in Natural and Engineered Barriers for Radioactive Waste Confinements, Nantes, 2010, p 103-124.

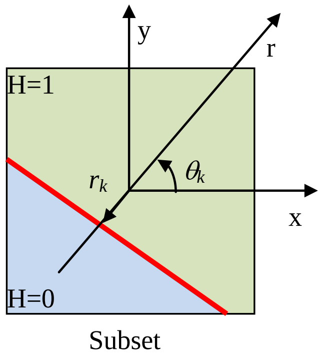

Figure 1: 2D Heaviside function description in the subset base.

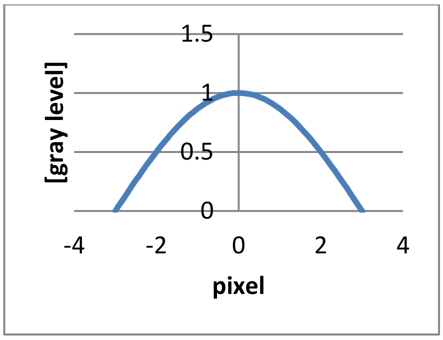

a) Speckle grain profile for a size of 6 pixels

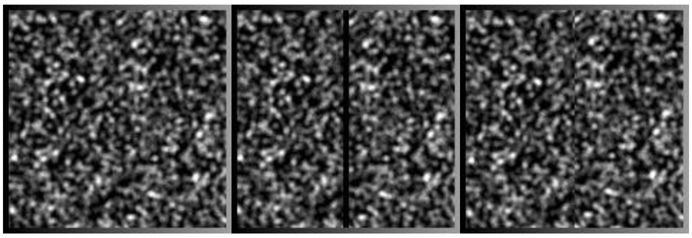

b) Reference

c) U=4 pixels Mode I

d) V=4 pixels Mode II

Figure 2: Simulated images for speckle grain size equal to six pixels, a) speckle grain profile, b) reference image, c) image obtained using a displacement of four pixels representing a mode I, d) image obtained using a displacement of four pixels mimicking a mode II.

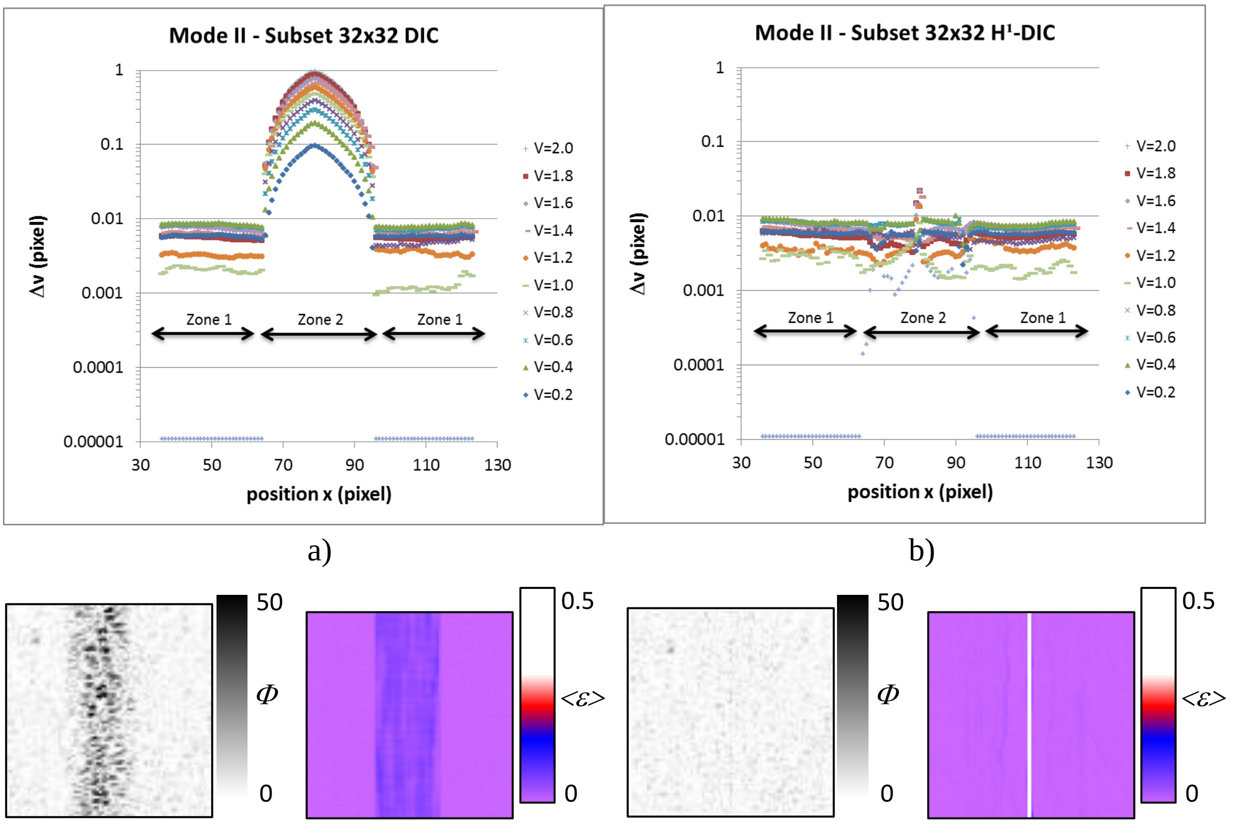

a) b)

c) d)

Figure 3: Displacement errors Δv for a sliding Mode II, calculated using images with a subset of 32×32 pixels^2 and imposed displacement jumps of $0.2 \leq V \leq 2$ pixels, using a) the classical DIC algorithm, b) the H^1-DIC algorithm. Local error map Φ in gray levels and pseudo strain map $<\varepsilon>$ for V=1.2 pixels using c) classical DIC algorithm, and d) H^1-DIC algorithm.

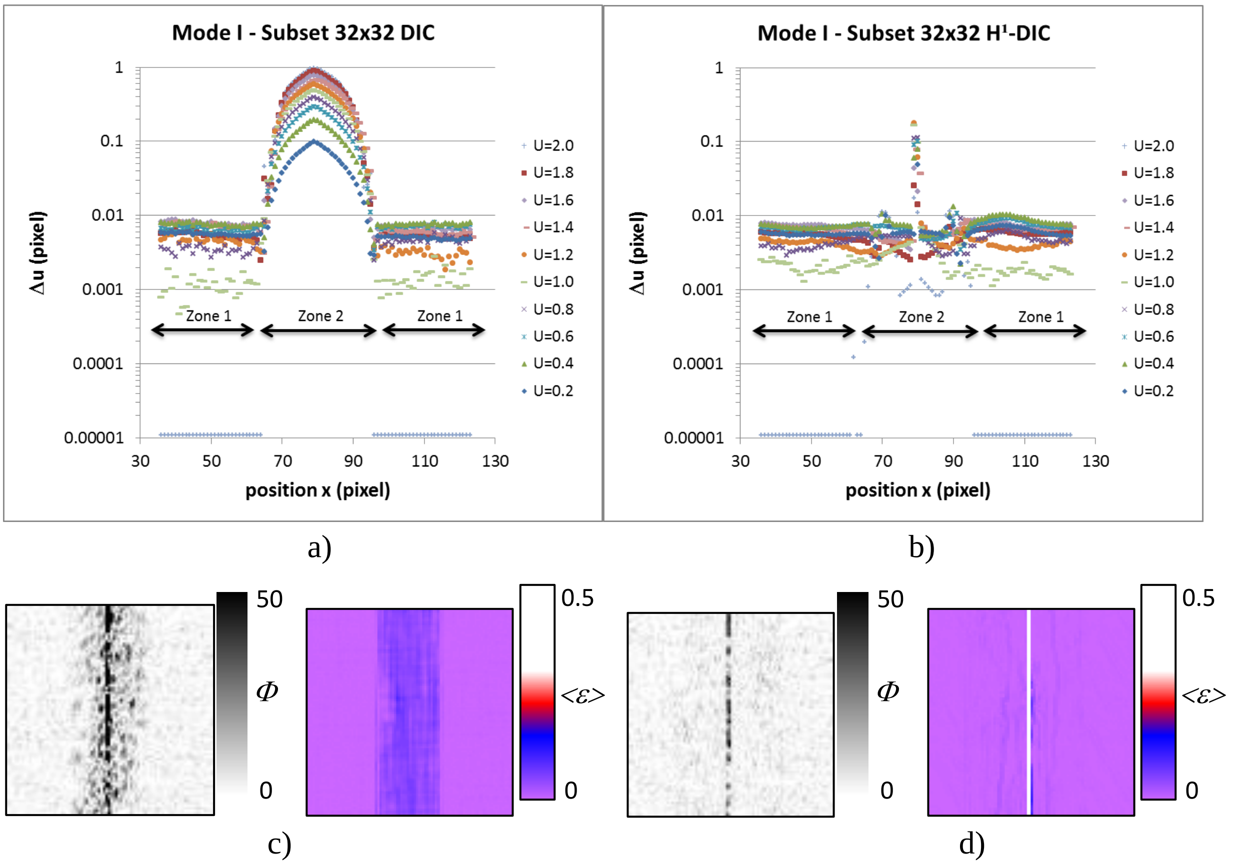

Figure 4: Displacement errors Δu for an opening Mode II, calculated using images with a subset of 32×32 pixels^2 and imposed displacement jumps of $0.2 \leq U \leq 2$ pixels, using a) the classical DIC algorithm, b) the H^1-DIC algorithm. Local error map Φ in gray levels and pseudo strain map $<\varepsilon>$ for U=1.2 pixels using c) classical DIC algorithm, and d) H^1-DIC algorithm.

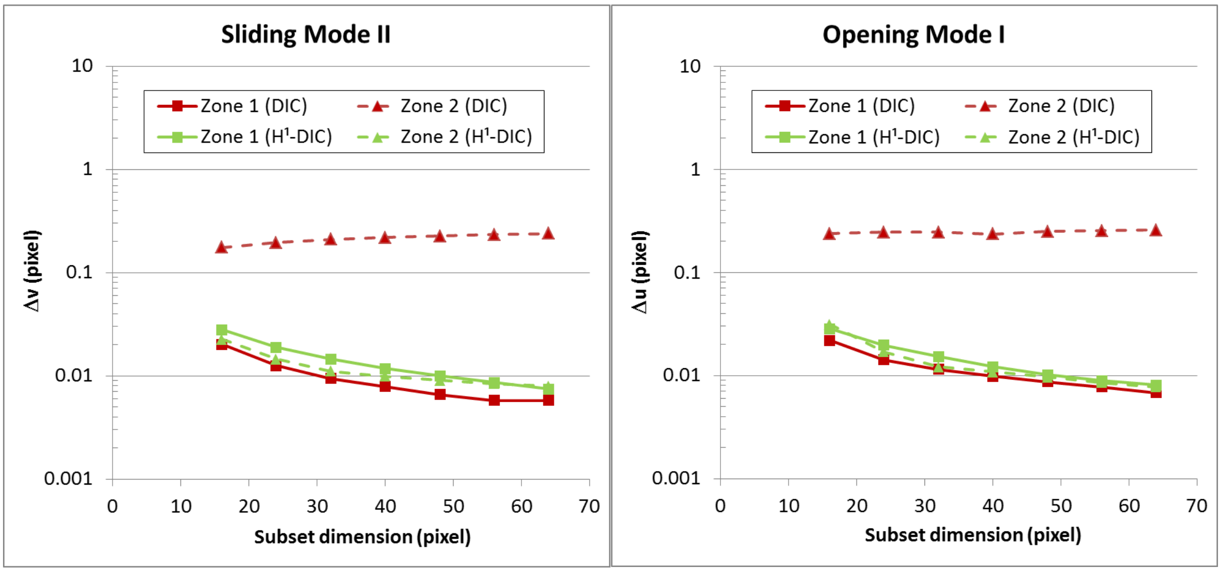

a) b)

Figure 5: Displacement errors calculated from simulated images with 10% noise, for different subset sizes and from two zones: Zone 1 far from the crack, and Zone 2 in the neighborhood of the crack. a) Δv is calculated for a sliding Mode II and a displacement jump V=1.2 pixels. b) Δu is calculated for an opening mode I and a displacement jump U=1.2 pixels.

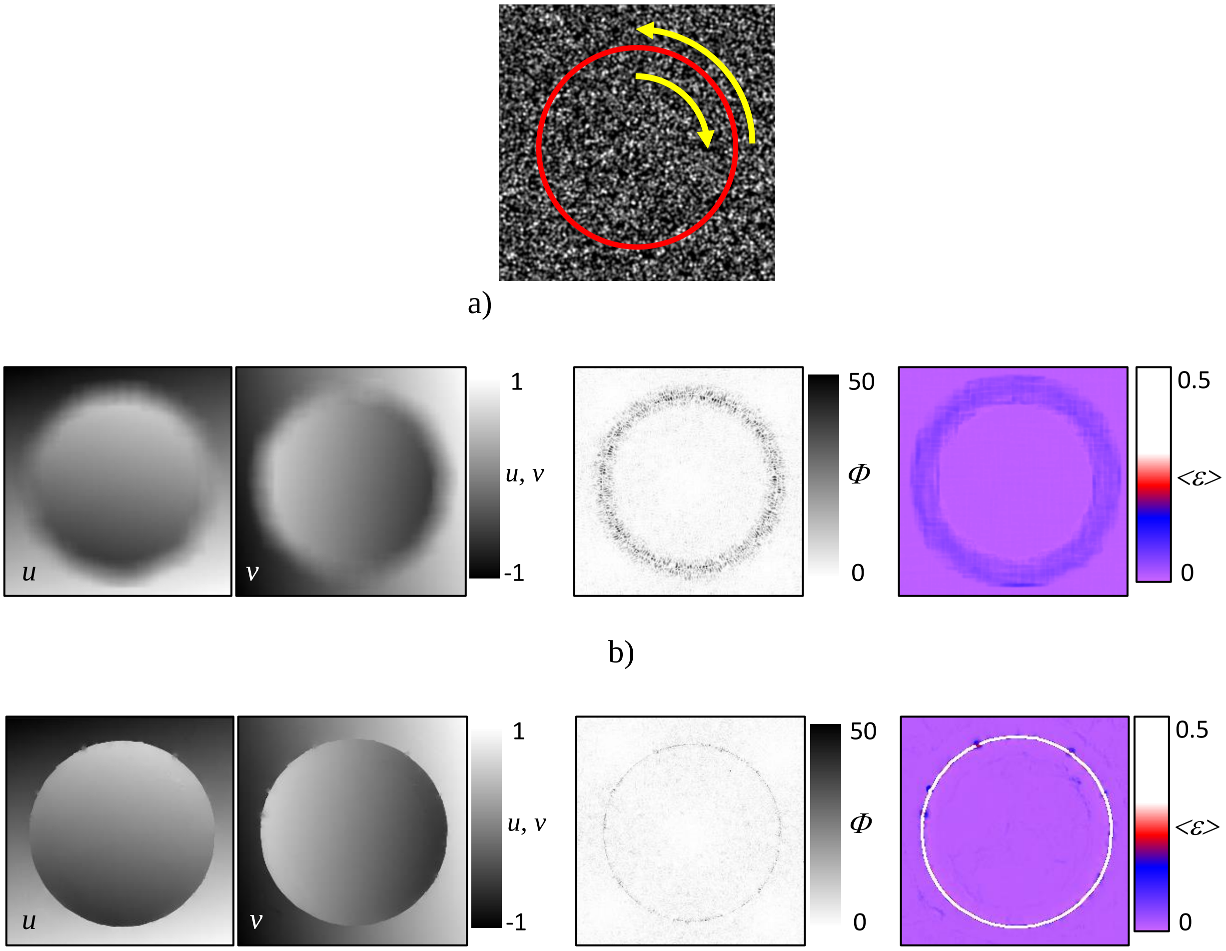

a)

b)

c)

Figure 6: a) Simulated image mimicking a sliding Mode II: rotation angle equal to ±0.23 degree. Displacements (u, v) in pixels, local error maps Φ in gray levels and pseudo strain $<\varepsilon>$ using b) classical DIC analysis, and c) H^1-DIC analysis.

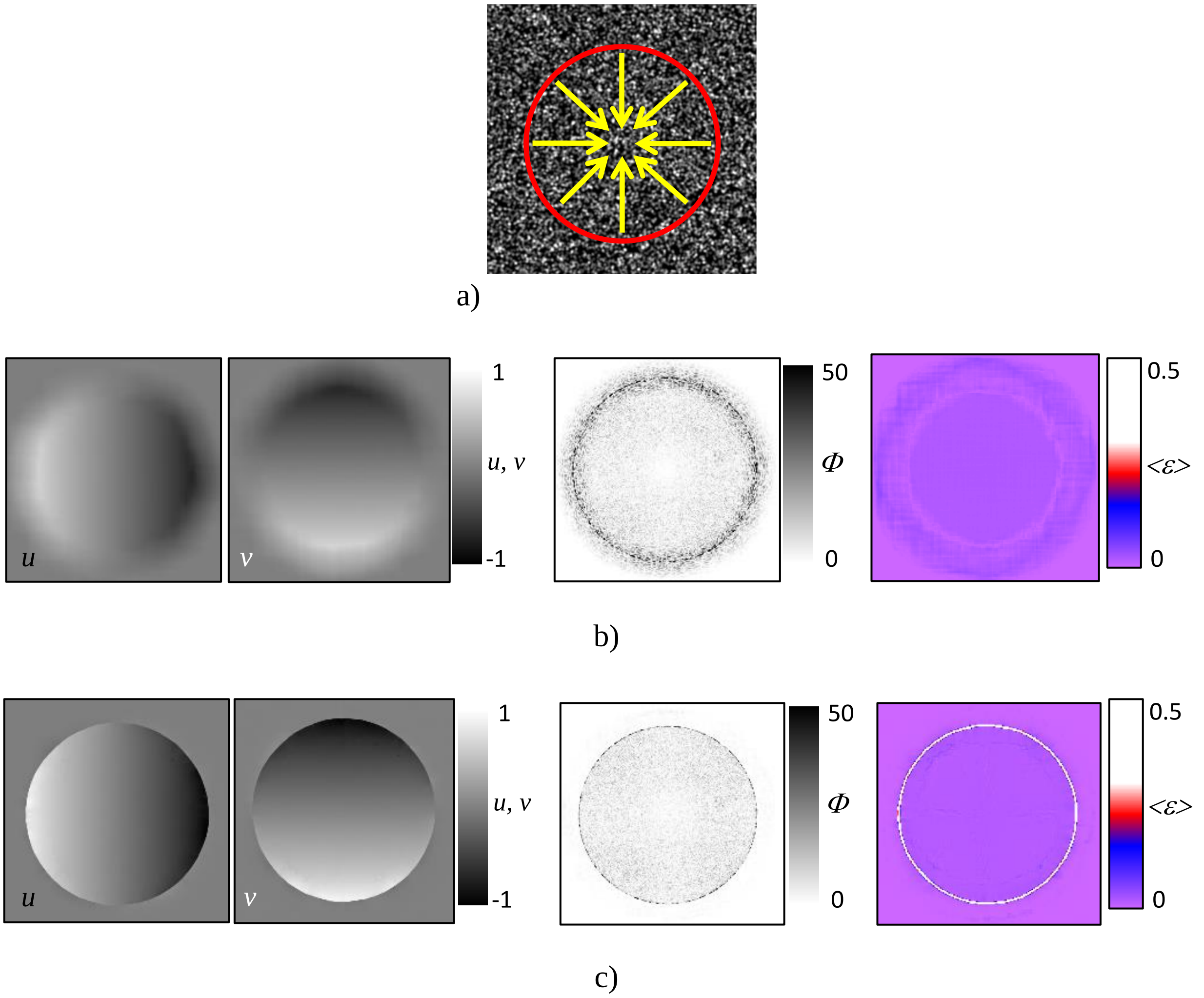

Figure 7: a) Simulated image mimicking an opening Mode I : radial strain equal to 2%. Displacements (u, v) in pixels, local error maps Φ in gray levels and pseudo strain <ε> using b) classical DIC analysis, and c) H^1-DIC analysis.

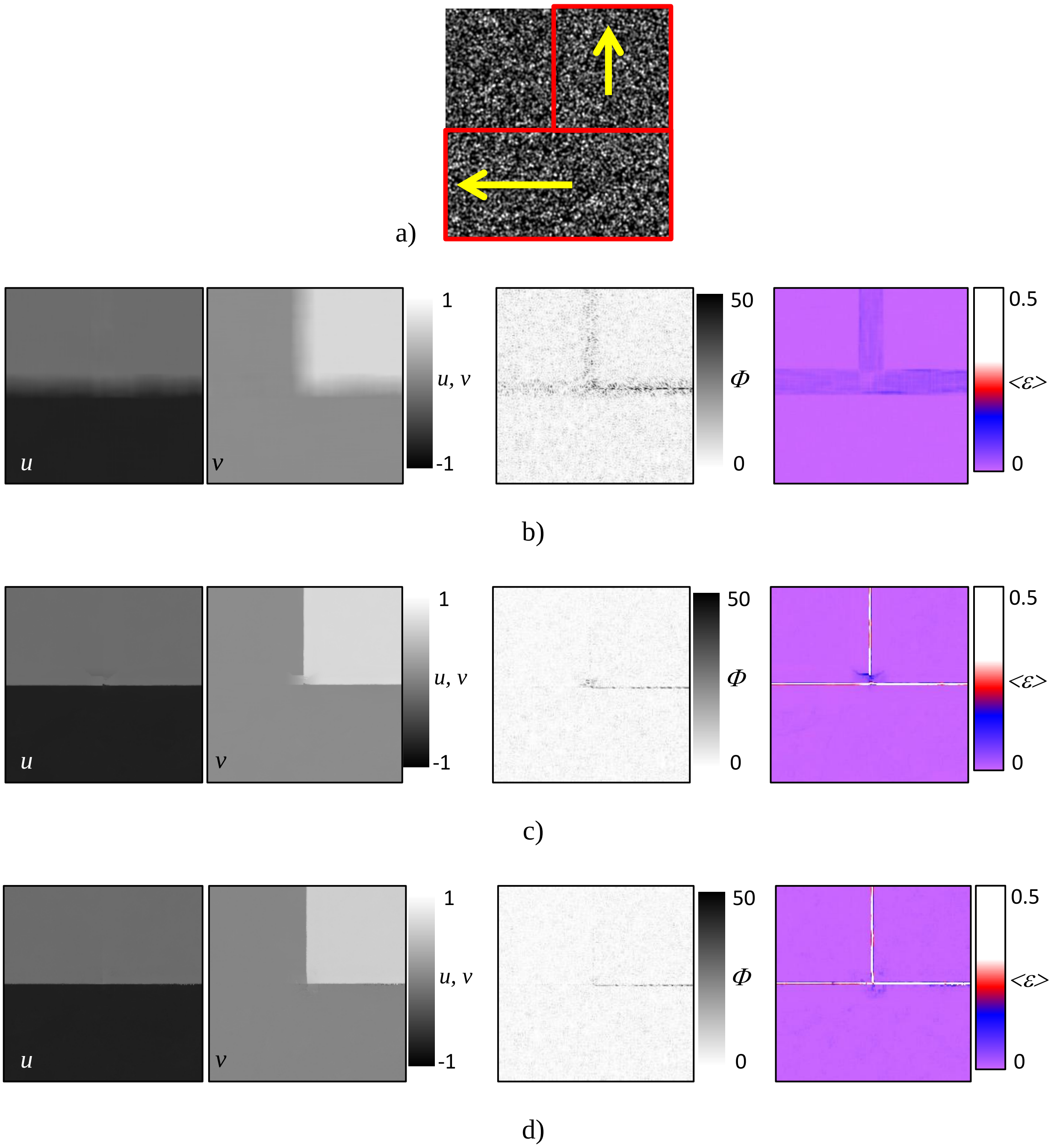

Figure 8: a) Simulated image mimicking a crack crossing: imposed displacement equal to ±0.8 pixel. Displacements (*u*, *v*) in pixels, local error maps Φ in gray levels and pseudo strain $<\varepsilon>$ using b) classical DIC analysis, c) H^1-DIC analysis, and d) H^2-DIC analysis.

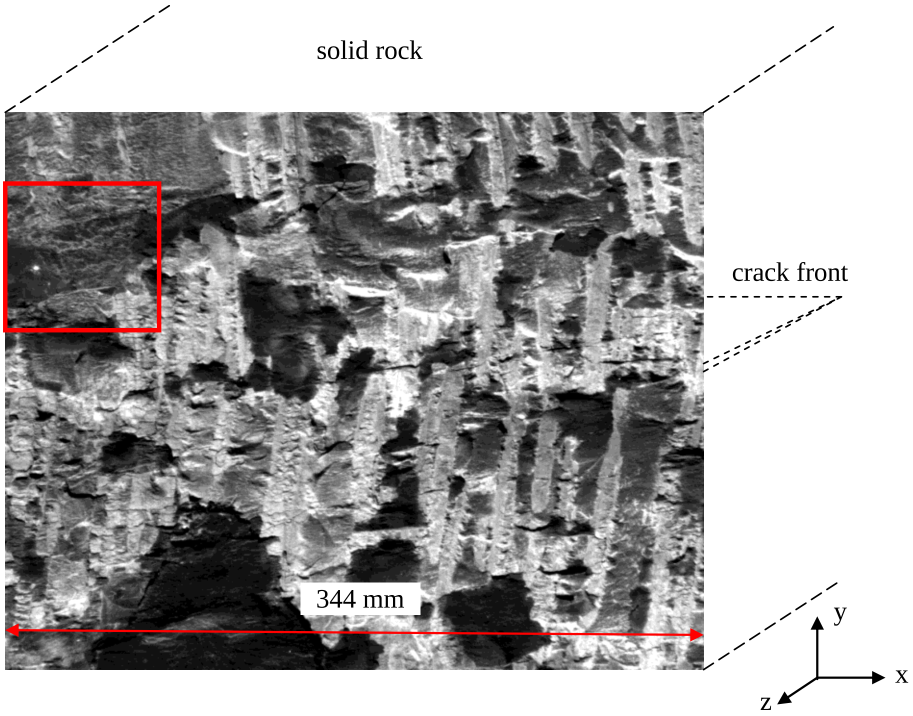

Figure 9: Image of the East96 gallery front at the Tournemire experimental station having a natural texture and the localization of the crack front. Red square defines the zone where the presented mechanical analysis is made

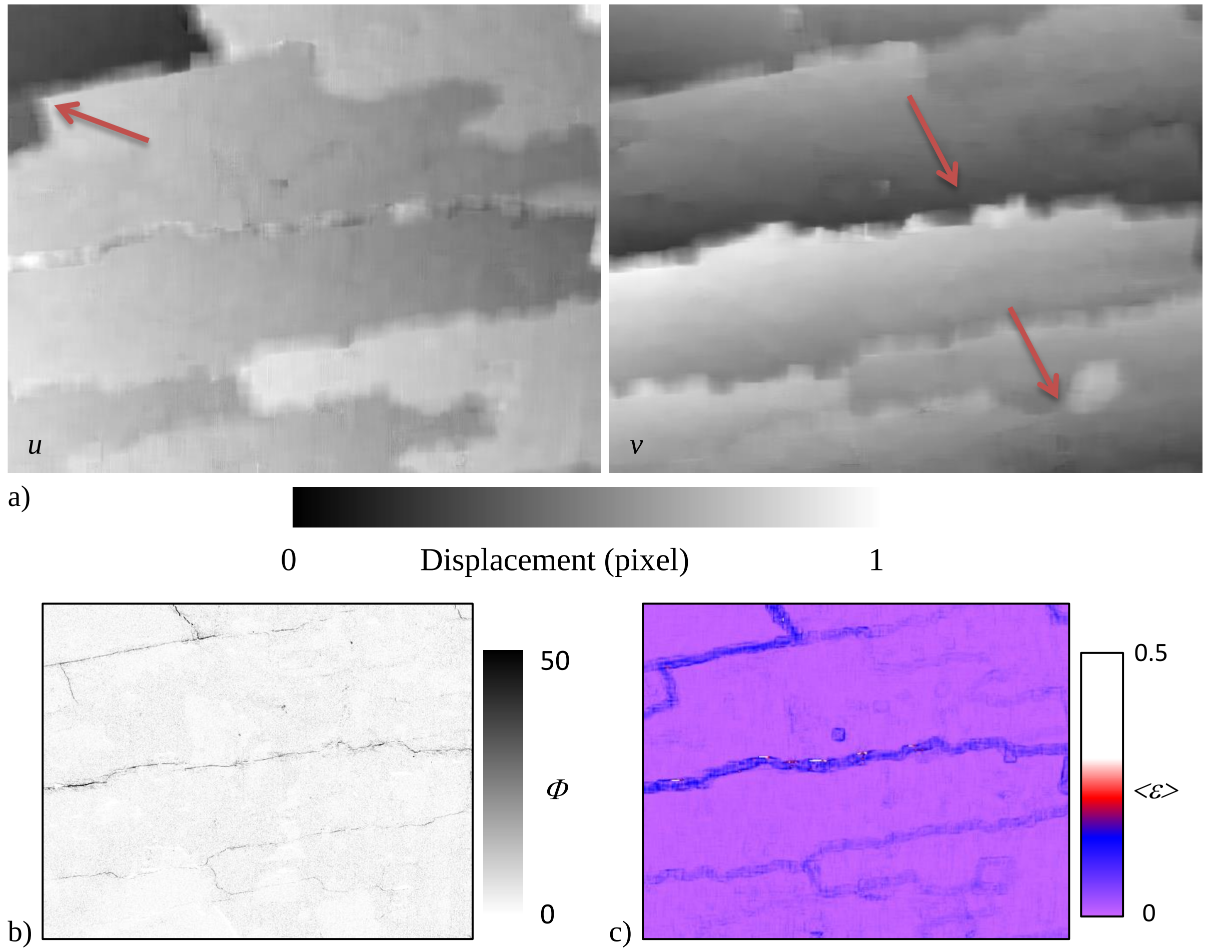

Figure 10: Results obtained using classical DIC procedure. a) Displacements (u, v) calculated with the classical DIC algorithm. b) Local error map Φ in gray level. c) Pseudo strain map $<\varepsilon>$. Red arrows represent some interesting details.

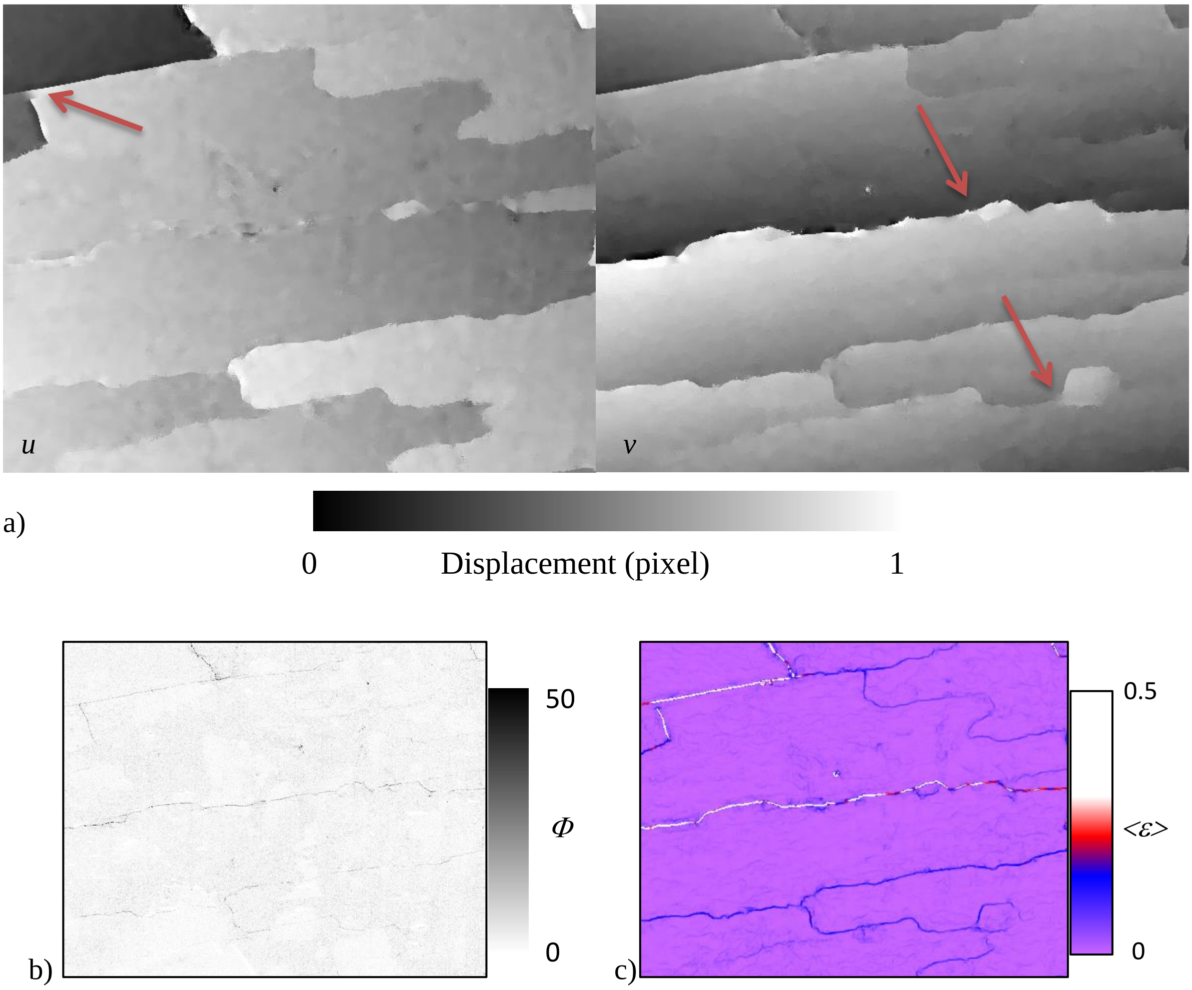

Figure 11: Results obtained using H^1-DIC algorithm. a) Displacements (u, v) calculated with the classical DIC algorithm. b) Local error map Φ in gray level. c) Pseudo strain map $<\varepsilon>$. Red arrows represent some interesting details.

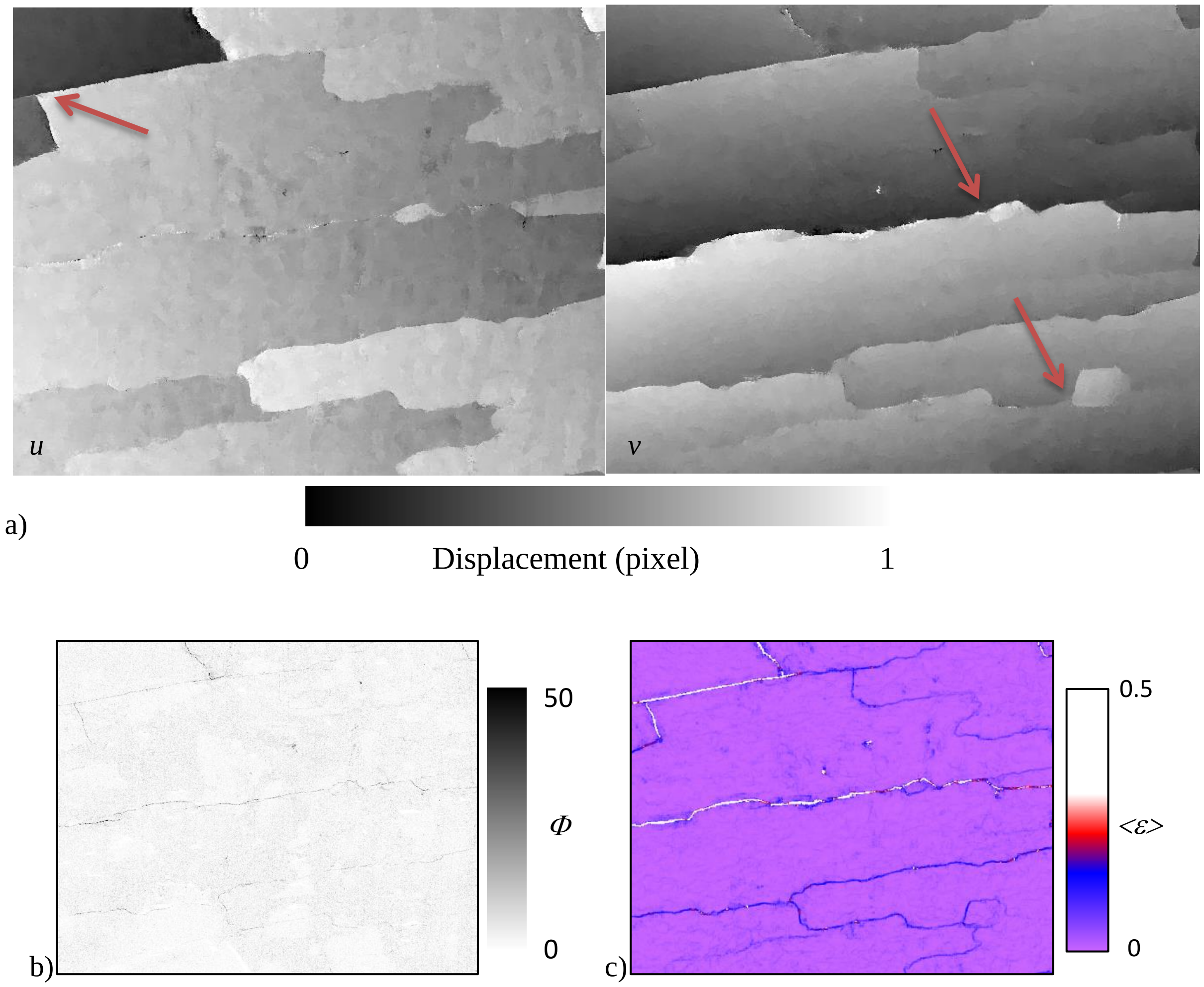

Figure 12: Results obtained using H^2-DIC algorithm. a) Displacements (u, v) calculated with the classical DIC algorithm. b) Local error map Φ in gray level. c) Pseudo strain map $<\varepsilon>$. Red arrows represent some interesting details.

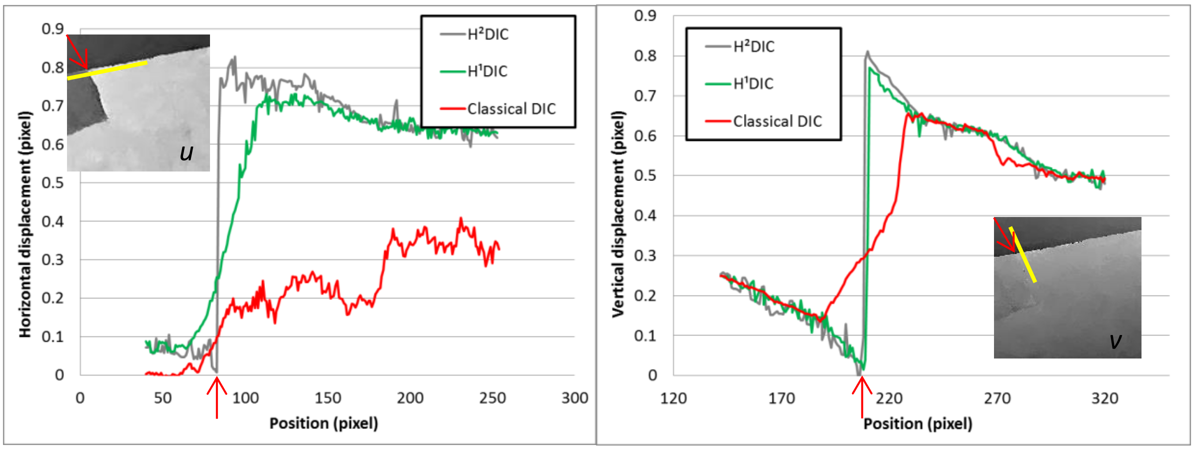

a) b)

Figure 13: a) Horizontal displacements and b) vertical displacements calculated at a crack crossing for each algorithm. Yellow lines represent the position of plotted data. Red arrows show the crack crossing position in pixel (81,210).

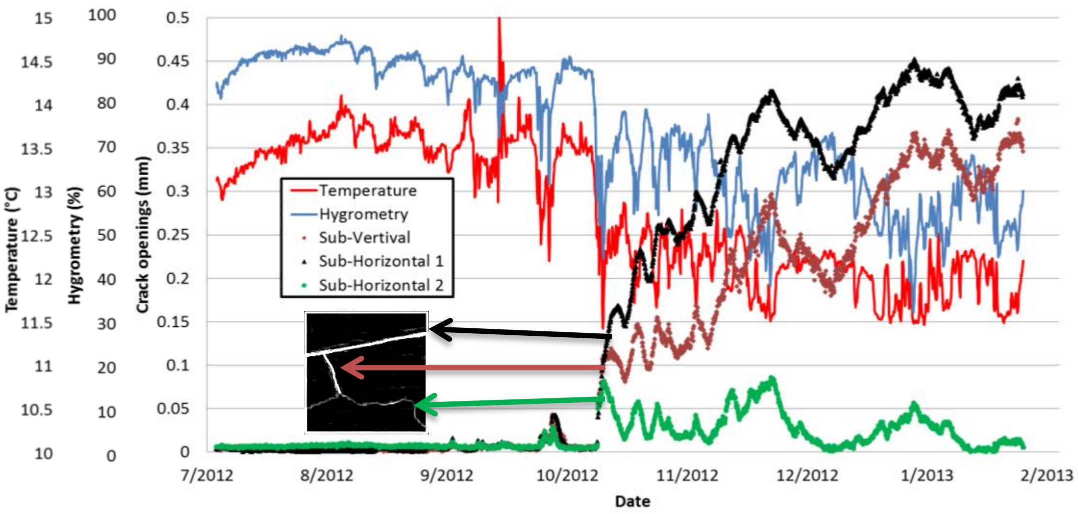

Figure 14: Sub-horizontal and sub-vertical crack opening, hygrometry and temperature evolutions versus to the time. Localization of the considered cracks on the pseudo strain map $<\varepsilon>$.

Implementation	Algorithm	computation rate (Msubsets/hour)	computation rate (subsets/second)
GPU (2688 cores)	Classical DIC	11.3	3140
	H^1-DIC	6.2	1720
	H^2-DIC	4	1110
CPU (1 core)	Classical DIC	0.1	30

Table 1: Comparison of computation rates vs. implementation for various algorithms.